

Defect-Driven Efficient Selective CO₂ Hydrogenation with Mo-Based **Clusters**

Jiajun Zhang, Kai Feng, Zhengwen Li, Bin Yang,* Binhang Yan,* and Kai Hong Luo*



Cite This: JACS Au 2023, 3, 2736-2748



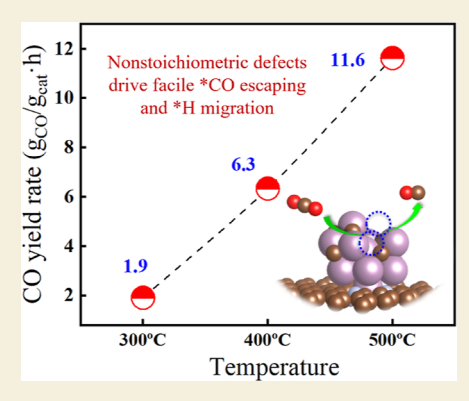
ACCESS I

III Metrics & More

Article Recommendations

Supporting Information

ABSTRACT: Synthetic fuels produced from CO₂ show promise in combating climate change. The reverse water gas shift (RWGS) reaction is the key to opening the CO₂ molecule, and CO serves as a versatile intermediate for creating various hydrocarbons. Mo-based catalysts are of great interest for RWGS reactions featured for their stability and strong metal-oxygen interactions. Our study identified Mo defects as the intrinsic origin of the high activity of cluster Mo₂C for CO₂-selective hydrogenation. Specifically, we found that defected Mo₂C clusters supported on nitrogen-doped graphene exhibited exceptional catalytic performance, attaining a reaction rate of 6.3 g_{CO}/g_{cat}/h at 400 °C with over 99% CO selectivity and good stability. Such a catalyst outperformed other Mo-based catalysts and noble metal-based catalysts in terms of facile dissociation of CO2, highly selective hydrogenation, and nonbarrier liberation of CO. Our study revealed that as a potential descriptor, the atomic magnetism linearly correlates to the liberation capacity of CO, and Mo defects facilitated product



desorption by reducing the magnetization of the adsorption site. On the other hand, the defects were effective in neutralizing the negative charges of surface hydrogen, which is crucial for selective hydrogenation. Finally, we have successfully demonstrated that the combination of a carbon support and the carbonization process synergistically serves as a feasible strategy for creating rich Mo defects, and biochar can be a low-cost alternative option for large-scale applications.

KEYWORDS: Mo₂C nanoparticle, synthesized fuels, RWGS reaction, atomic magnetism, selective hydrogenation

1. INTRODUCTION

CO₂ hydrogenation to produce synthetic fuels is an important strategy to realize the goal of "net zero" emission based on existing energy infrastructures. CO is an important intermediate from CO₂ hydrogenation and can be used directly as fuel or as feedstock in tandem reactions for a diverse range of fuel products.² A variety of noble metal-based catalysts have been developed for reverse water gas shift (RWGS) reactions in recent years, 3-8 but their high cost poses insurmountable challenges for commercial implementation. Non-noble metals for the RWGS reaction normally have poor activity and selectivity, especially at low temperatures, but there are exceptions, being highly dependent on the fine regulation of the local electronic structures for the active sites.9-13

For example, Co-based catalysts are always deemed to fail to catalyze the RWGS reaction, 14 but the nitrogen coordinated single atom Co performed almost 100% selectivity to CO with over 50% conversion during CO2 hydrogenation, with a gas hourly space velocity (GHSV) of 6000 mL/(g h) and a carbon-to-hydrogen ratio of 4:1, providing a new strategy for designing base metal-based RWGS catalysts. 15 CeO2 with surface regulation also exhibited a high activity in the RWGS reaction. Dedicated oxygen defects on the catalysts realized a balance between CO₂ dissociation and surface hydrogenation,

delivering the best activity. 16 Native point defects in vanadium carbide strengthened the electronic interactions between the reactant and the catalyst, facilitating the RWGS reaction. 17 Tailored multicomponent catalysts, including Cu and Fe alloys, were also commonly seen to promote the RWGS performance, 18 where Cu promotes CO₂ activation, and normally leads to the formate mechanism for the hydrogenation, while Fe improves the thermal stability and was found to favor redox mechanism for hydrogenation. Alkali metals were frequently doped to improve CO2 adsorption and suppress excess adsorption of H₂, leading to methanation. ^{19,20}

Mo-based catalysts have shown outstanding performance in the RWGS reaction among non-noble catalysts. Molybdenum carbides (Mo₂C), nitrides (Mo₂N), phosphides (MoP), and metallic molybdenum (Mo) are of particular interest for the selective hydrogenation of CO2. They are favored due to their ability to form strong metal-oxygen bonds and stability, which are crucial for the RWGS reaction.²¹ Nanoparticles have been

Received: April 26, 2023 Revised: August 25, 2023 Accepted: August 30, 2023 Published: September 15, 2023





shown to have better catalytic performance compared to extended surfaces in terms of adsorption and dissociation of CO_2 , as well as hydrogen diffusion. ^{22,23}

MoP supported on SiO₂ has shown fully CO-selective capability at 450 °C and was shown to remain stable for over 22 h.²⁴ Hexagonal 2D-Mo₂C catalysts exhibited higher activity than β -Mo₂C for CO formation by a rate of roughly 1180 mg/ h/g_{cat} at 230 °C, with a H₂ to CO₂ ratio of 3:1. This was benefited from the unsaturated surface attained during the preparation from Mo₂CT_x with abundant surface termination groups of O, OH, and F. 25 Mo₂N has also been found to be active and outperform W2N and NbN for CO2 hydrogenation with high CO selectivity. The interstitial vacancies in the crystal could be reversibly filled with the oxygen, facilitating CO₂ dissociation and hydrogenation through the redox mechanism.²⁶ With the addition of Pt, MoO₃ was found to form MoO_x-rich O vacancies over Mo₂N, and the metalvacancy synergistic sites were much more active for the RWGS reaction. The catalyst realized nearly 20% conversion in a high GHSV of 3,000,000 mL/g/h with a carbon-to-hydrogen ratio of 1:3.²⁷ The insertion of N into the interstitial site of CoMo alloy was also observed to promote the catalytic performance for the RWGS reaction. H₂ experiences dissociative adsorption on N, and Mo becomes more electron deficient, such that it is beneficial for CO desorption.²⁸ A single-atom catalyst of Mo coordinated by N demonstrated very high selectivity to CO due to the lack of an atomic ensemble. It gives rise to exothermic desorption of product molecules even at low temperature of 300 °C, and the conversion of CO₂ reached 24% at 500 °C with a C/H ratio of 1:3.29,30

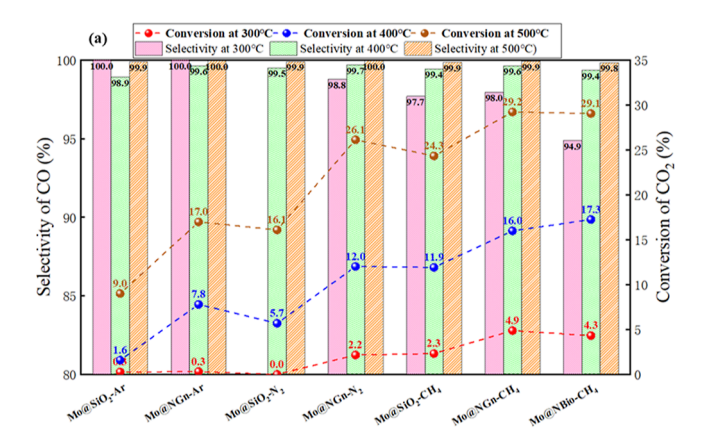
Mo-based catalysts, including their alloys, have attracted significant interest in recent years due to their high performance in selective hydrogenation. However, the origin of their activity, especially for cluster catalysts, has not been fully understood, despite numerous efforts to establish more efficient low-temperature catalytic systems for the RWGS reaction. This study proposed that Mo defects are the decisive factor for the superior activity of Mo₂C cluster in the selective hydrogenation to CO2. Based on this, a facile strategy is demonstrated to improve the intrinsic catalytic activity. We also report on the mechanisms underlying the high activity of the defected Mo clusters, including defect-induced neutralization of surface H charges to promote selective hydrogenation, and the affinity between product desorption capacity and defect-induced atomic magnetization. These mechanisms are supported by multiscale modeling results and experimental evidence.

2. RESULTS AND DISCUSSION

2.1. Performance of Mo-Based Catalysts under RWGS Conditions

The catalytic performance of a variety of Mo-based catalysts was evaluated at 300, 400, and 500 $^{\circ}$ C in a sequential test. Specifically, we compared Mo-based cluster catalysts prepared in the atmosphere of argon and hydrogen (reduction, Mo), nitrogen and hydrogen (nitrogenation, Mo₂N), and methane and hydrogen (carbonization, Mo₂C), respectively. Supports of nitrogen-doped graphene (NGn), nitrogen-doped biochar (NBiochar), and SiO₂ were tested to reveal their effects on the catalytic performance, as shown in Figure 1a.

We observed that the conversion of CO₂ generally increased with temperature, and the catalysts pretreated by carbonization



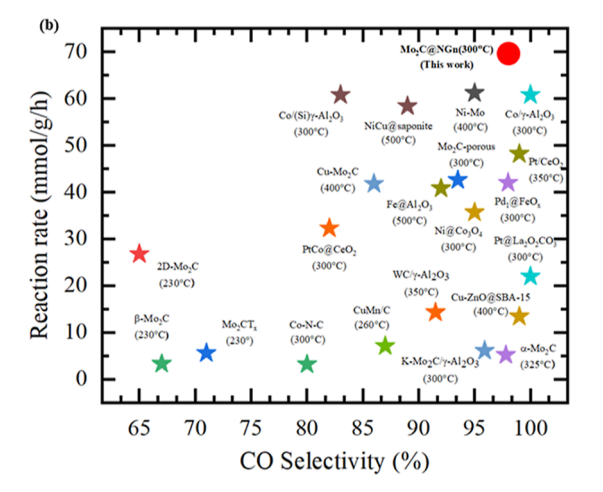


Figure 1. (a) Conversion of CO_2 and selectivity of CO for the catalysts of the Mo support on carbon and SiO_2 pretreated under reduction, nitrogenation, and carbonization, respectively, at 300 °C/400 °C/500 °C (GHSV = 140,000 mL/g/h, mol_{CO_2}/mol_{H_2} = 1:2). (b) Summary of the performance under RWGS conditions for the reported catalysts.

always gave rise to better catalytic activity. The conversion of CO₂ reached 24.3% over Mo@SiO₂-CH₄ at 500 °C, 29.2% over Mo@NGn-CH4 at the same temperature, and 16.0% at 400 °C and 4.9% at 300 °C. The peak conversion for the nitrogenized Mo@NGn was 26.1% at 500 °C and only 17.0% for the reduced catalyst. The selectivity of CO in the RWGS reaction was almost 100% at 500 °C and not much affected by the catalyst preparation atmosphere. Only slight changes caused by temperature were observed for the nitrogenized catalysts and carbonized catalysts. In contrast, we observed the non-negligible effects of the support on catalytic activity; carbon support gave rise to better catalytic activity compared to SiO₂, wherein the nitrogen doping may play a key role in stabilizing the metal-based nanoparticles.^{31–33} By comparing the nitrogenized Mo@NGn and Mo@SiO2, a 10.0% higher conversion was observed at 500 °C and a 6.3% rise at 400 °C. For the catalysts prepared in methane, the conversion over the carbon support was about two-fold of that over Mo@SiO2 at 300 °C. We concluded from the experimental data that the Mo-based catalysts prepared under the carbonization conditions result in the best catalytic performance for the RWGS reaction, and carbon supports would further promote the catalytic activity.

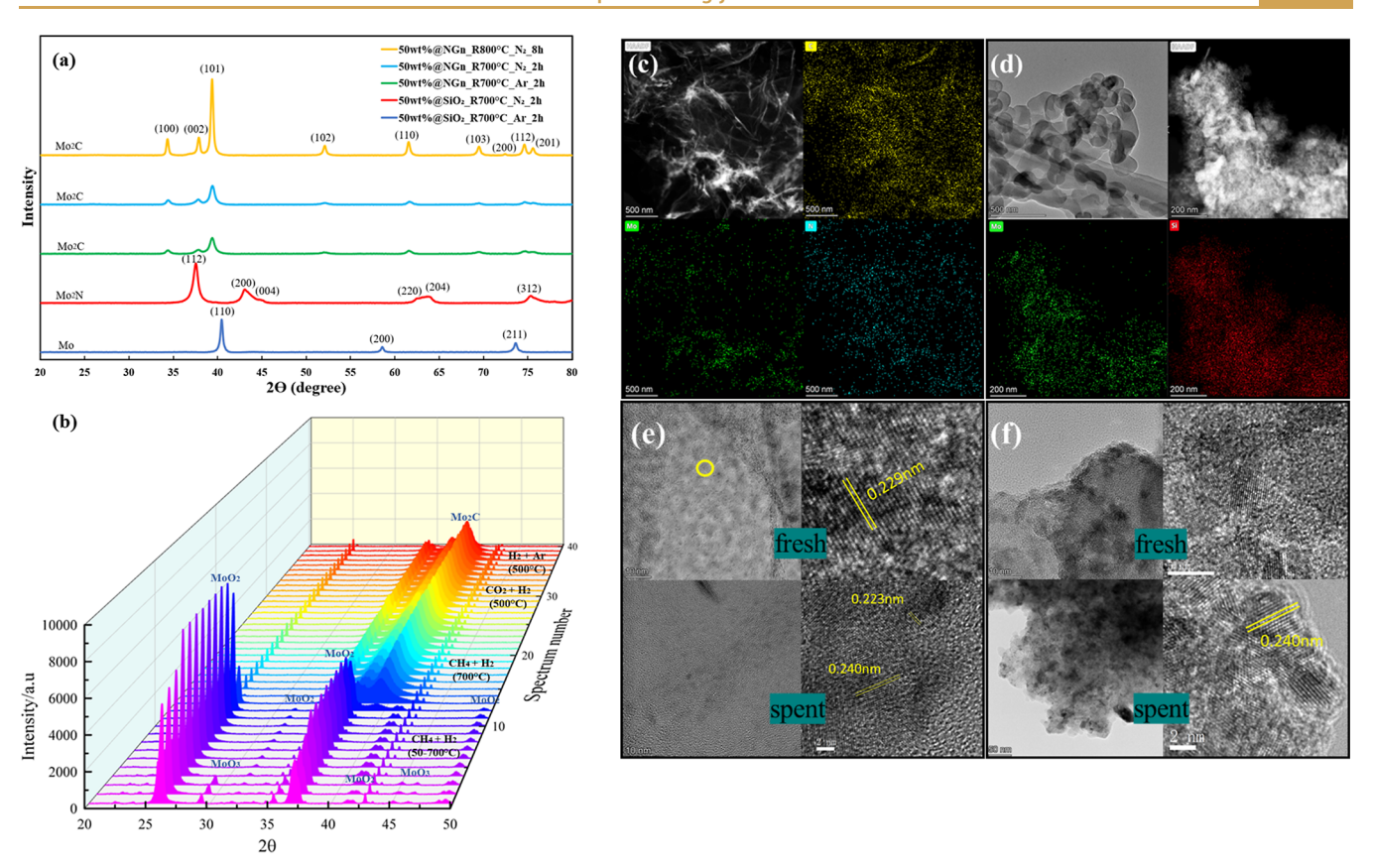


Figure 2. (a) XRD spectra of the Mo-based catalysts. (b) In situ XRD spectra of Mo@NGn during carbonization, RWGS reaction, and reductive treatment. HAADF images and EDS elemental mapping images of (c) fresh Mo@NGn-CH₄ and (d) Mo₂C@SiO₂-CH₄. HD-TEM images for fresh and spent catalysts (e) Mo₂C@NGn-CH₄ and (f) Mo₂C@SiO₂-CH₄.

The normalized catalytic performance of reported metalbased catalysts under the low-temperature RWGS conditions was compared with Mo@NGn-CH₄ and is shown in Figure 1b and Table S1. We observed that Mo@NGn-CH₄ is especially outstanding in terms of catalytic activity and CO selectivity among recently reported single-metal-based catalysts and even noble metal-based catalysts, 25,34 and its low-temperature performance is superior compared to other Mo family catalysts including α/β -Mo₂C, 2D-Mo₂C, and porous Mo₂C, attaining a CO₂ reaction rate of 69 mmol/g/h and a CO selectivity of 98% (yield rate of 1904 mg_{CO}/g/h) at 300 °C, and a reaction rate of 227 mmol/g/h and selectivity of 99.6% (yield rate of 6331 mg_{CO}/g/h) at 400 °C, and 415 mmol/g/h for reaction rate and 99.9% for selectivity (yield rate of 11,620 mg_{CO}/g/h) at 500 °C, indicating high atom usage efficiency of Mo₂C@NGn. We also prepared biochar as an alternative carbon support, which has been found to give rise to CO₂ conversion as NGn. Despite slightly lower selectivity of CO at 300 °C, biochar finds its preponderance of benefit in terms of economy.

To clearly identify the active species on the catalysts, we implemented X-ray diffraction (XRD) tests on the above catalysts. The results in Figure 2a reveal that no matter what treatment atmosphere was applied during catalyst preparation over the NGn support, Mo₂C is the actual active site for all the catalysts supported on carbon, as evidenced by the characteristic peaks at 34.3, 37.7, 39.3, 51.9, 61.5, 69.1, 72.4, 74.5, and 75.5° for (1 0 0), (0 0 2), (1 0 1), (1 0 2), (1 1 0), (1 0 3), (2 0 0), (1 1 2), and (2 0 1) facets for $C_{1.02}Mo_{1.98}$, respectively (PDF#65-8364). Besides, the results also reveal that longer treatment and higher temperature contributed to a

higher peak intensity of Mo₂C, implying that the interaction between the carbon support and Mo is strengthened with a larger size of clusters. To verify the carbon support-metal interaction, we implemented additional XRD tests to the SiO₂supported catalysts of Mo@SiO₂-N₂ and Mo@SiO₂-Ar. Not surprisingly, we merely observed the characteristic peaks at $37.7 \text{ and } 43.0^{\circ} \text{ for Mo}_{2}N (1 \ 1 \ 2) \text{ and } (2 \ 0 \ 0) \text{ for Mo}_{@}SiO_{2}-N_{2}$ (PDF#75-1150), and the peaks at 40.5, 58.7, and 73.7° are of metallic Mo (1 1 0), (2 0 0), and (2 1 1), respectively, for Mo@SiO2-Ar (PDF#89-5023), 38,39 as shown in Figure 2a. Considering the surface reaction results, we confirm that Mo₂C has superior catalytic behavior over Mo₂N or Mo in the RWGS reaction and that the carbon support is vital for Mo₂C formation in the carbonization process. We then carried out an in situ XRD test to Mo@NGn-CH₄ (known as Mo₂C@NGn) to reveal its full-life evolution, as shown in Figure 2b, and the corresponding species for the main peaks are labeled. During the carbonization period, main characteristic peaks of the catalyst precursor were found, namely, the peak at 26.0° for MoO_2 (1 1 0) and 36.9° for MoO_2 (0 2 0), together with some other small peaks at 31.7, 41.3, and 49.4° (PDF#73-1249).40 Besides, the peaks of 29.4, 45.4, 46.6, and 48.9° are identified as MoO₃ (PDF#21-0569).⁴¹ After Mo₂C formation, it was identified with the same peaks as those identified in the ex situ XRD test. Besides, some constant tiny peaks at 25.6, 35.1, 42.7, and 43.2° were also noticed, and they are identified to be the component material (Al₂O₃) of the crucible exposed to the Xray during the text (PDF#75-1864 & PDF#34-0493). 42,43 During the two-stage carbonization process in the CH₄ and H₂ atmosphere, we observed an intensity increase for the

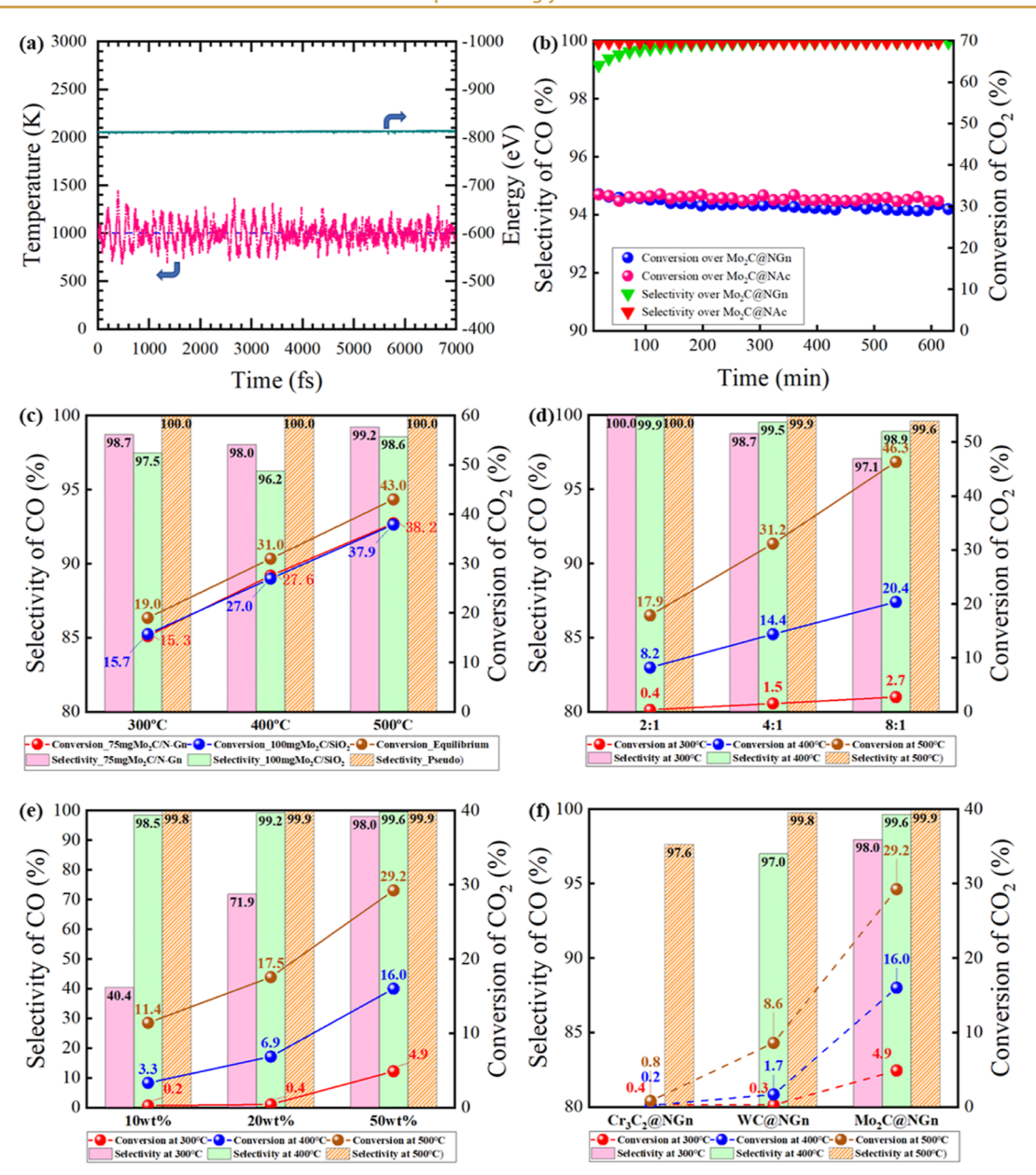


Figure 3. (a) Stability of the active site for $Mo_2C@NGn$ evaluated by AIMD at 800 °C. (b) Stability of the $Mo_2C@NGn$ catalyst under RWGS reaction conditions at 500 °C. The performance of $Mo_2C@NGn$ with various (c) temperatures (GHSV = 16,000 and 12,000 mL/g/h for $Mo_2C@NGn$ and $Mo_2C@SiO_2$ respectively, mol_{CO_2}/mol_{H_2} = 1:2). (d) Hydrogen to carbon ratios in hydrogenation (GHSV = 318,000 mL/g/h). (e), Loading ratios. (f) VIB metal carbides under RWGS conditions (GHSV = 140,000 mL/g/h, mol_{CO_2}/mol_{H_2} = 1:2 for e,f).

precursor peaks before being fully eliminated, indicating growth of the particle size of the metal oxide particles which may experience a redispersion during the carbonization process. 44 A constant signal for Mo₂C appeared at nearly 700 °C at the end of the heating up stage. The results also revealed that Mo₂C active site remained stable throughout the RWGS reaction conditions at 500 °C, without any oxidation or phase changes.⁴⁵ When applying only H₂ and Ar instead of the reactive atmosphere, we found that Mo₂C@NGn would still remain stable in such a reductive atmosphere, further confirming the stability of the active site. From the above tests, we can also confirm that Mo₂C was the sole active site in our experiments with CO₂ hydrogenation. Transmission electron microscopy (TEM) was adopted to reveal the appearance of the as-obtained Mo₂C-based catalysts and spent catalysts. The high-angle annular dark-field (HAADF)

image in Figure 2c demonstrated film-like structure of the graphene-supported catalyst. Mapping images by energy-dispersive X-ray spectroscopy (EDS) for Mo₂C@NGn show the homogeneous distribution of Mo on NGn. Figure 2d shows the global appearance and EDS mapping images of Mo₂C@SiO₂. Similar distributions of Mo species were observed on the SiO₂ support. Besides, high-resolution (HD) TEM images in Figure 2e,f show Mo₂C species on the respective NGn and SiO₂ support before and after the RWGS reaction, indicating the chemical stability of the active species throughout the reaction. We also observed that the Mo₂C particles over NGn show diameters ranging from 1 to 5 nm, smaller than those over SiO₂ (Figure S2).

As the most active catalyst, the stability of Mo₂C@NGn was directly evaluated by respective DFT modeling and catalytic performance under RWGS conditions. The cluster model (as

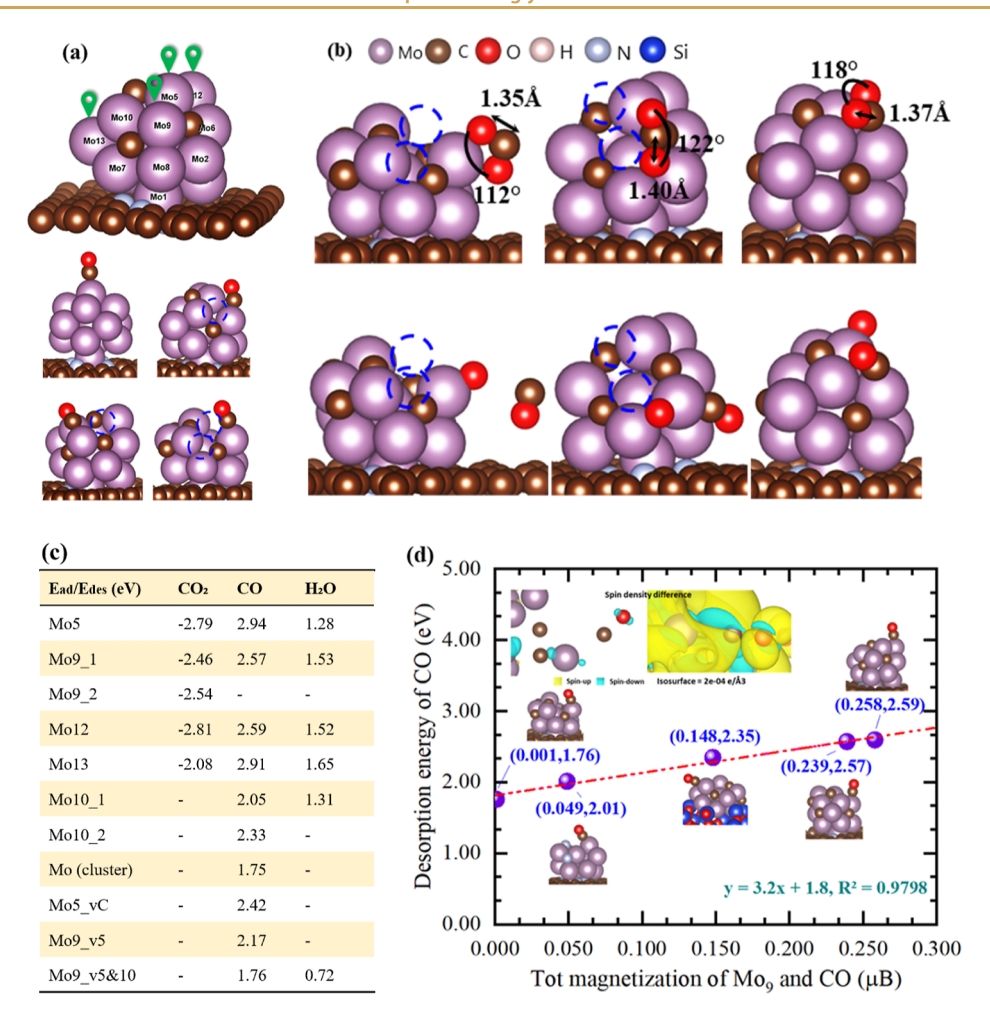


Figure 4. a) Models of the intact cluster and adsorption configurations of CO on $Mo_2C@NGn$ with various types of Mo defects (in blue dashed line circles). (b) Adsorption configurations of CO_2 on the defected $Mo_2C@NGn$ and intact catalyst. (c) Summary of the adsorption energy of CO_2 , CO_3 , and H_2O_3 . (d) Magnetization (net spin) of the adsorption site atom as a function of and desorption energy of CO_3 .

shown in Figure S3a) was established and simulated at 800 °C by ab initio molecule dynamics (AIMD) for 7 ps, and the total enthalpy and temperature were monitored and are demonstrated in Figure 3a. The results indicate that the cluster active site remains dynamically stable under the high temperature throughout the modeling period, where doped nitrogen may play a key role in stabilizing the cluster particle. 46,47 The fresh catalyst was tested in an experiment under the RWGS reaction conditions at 500 °C for over 10 h. Results reveal that CO selectivity and conversion of CO2 could both keep steady at nearly 100 and 30%, respectively. Besides, we also found from the test that the cluster supported on biochar could retain the same stability as the graphene-supported catalyst (Figure 3b). The stability of the catalyst is also confirmed by the strong interaction between the Mo₂C cluster and NGn observed in the DFT modeling (Figure S3c), as well as the highly dispersed small particles observed in the TEM images.

We then implemented further reaction studies to clearly demonstrate the effect of the active site—support interaction on the low temperature catalytic performance. The results in Figure 3c indicate the conversion of CO₂ over Mo₂C@NGn reached 15.3% at 300 °C (38.2% at 500 °C and 27.6% at 400 °C) with a GHSV of 16,000 mL/h/g, approaching the conversion of chemical equilibrium, and the selectivity of CO is all above 98%. The same conversion needed 30 wt % more

Mo₂C@SiO₂ with lower selectivity, indicating the superior synergistic effect between the carbon support and Mo. More experiments were carried out to reveal the effects of the H₂ to CO₂ ratio on the hydrogenation over Mo₂C@NGn (Figure 3d), where the GHSV was kept constant for these three tests. The results show that the catalyst maintains a high CO selectivity of 97% at 300 °C even under a H-to-C ratio of 8:1, implying the outstanding capacity of the catalyst in selective hydrogenation in RWGS reactions. We have also probed the effects of the metal loading ratio on the NGn support. Figure 3 confirms that the catalytic performance is in positive correlation with the loading ratio of Mo before 50 wt %. Other group-VIB-metal-based catalysts of Cr₃C₂ and WC were tested under identical RWGS reaction conditions (Figure 3f). The corresponding nitrogenized catalysts were also investigated in a variety of working conditions (Figure S4). The results confirm the exceptional catalytic performance of Mo₂C@NGn in all of the tested RWGS conditions.

2.2. Mechanism for Efficient RWGS Reaction over Mo₂C@NGn

The underlying mechanism of the selective hydrogenation over $Mo_2C@NGn$ was investigated with DFT modeling. The intact cluster model is demonstrated in Figure 4a. Potential adsorption sites to the electrophilic attack on intact clusters (labeled in green) were identified by Kukui analysis (Figure

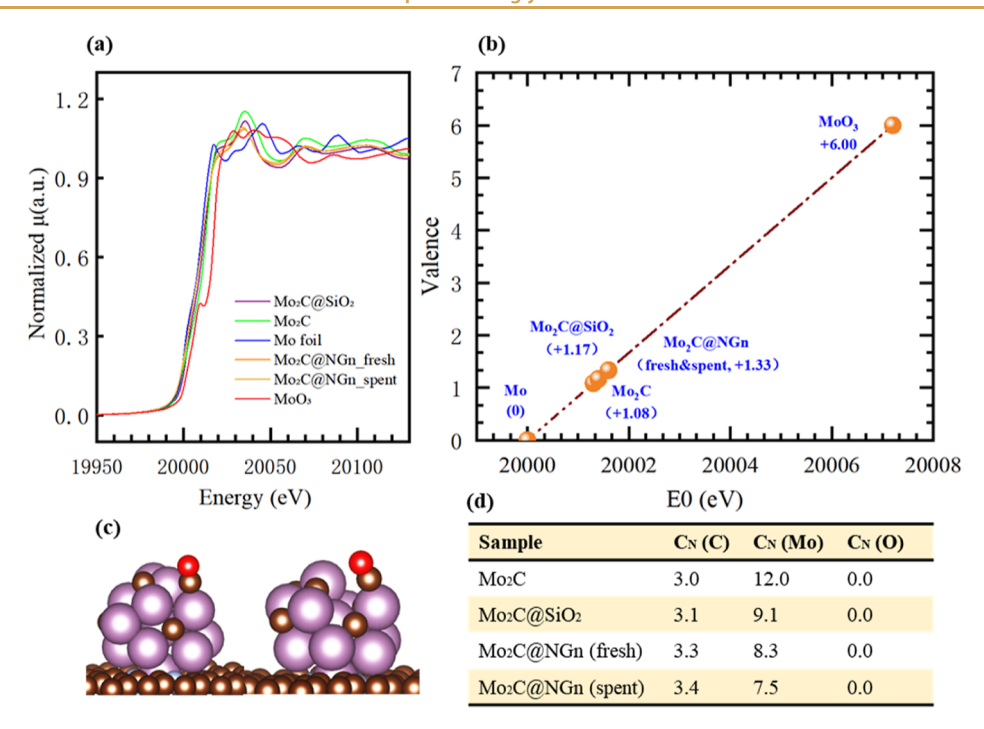


Figure 5. a) Mo K-edge XANES for the Mo-based catalysts. (b) Averaged valence of Mo in the specimens of Mo₂C@SiO₂, Mo₂C@NGn (fresh), and Mo₂C@NGn (spent) estimated with standard samples of Mo₂C and metallic Mo. (c) Models of the intact and defected cluster of Mo₂C supported on NGn. (d) Averaged coordination numbers of central Mo in the specimens of standard Mo₂C, Mo₂C@SiO₂, Mo₂C@NGn (fresh), and Mo₂C@NGn (spent).

S5). The adsorption energies of CO₂ and the desorption energies of CO and H2O on the potential active sites were calculated. The adsorption energies for the most stable configuration on each site are shown in Figure 4c. The results reveal CO desorption energy on intact Mo₂C cluster ranging from 2.05 to 2.94 eV, and the corresponding CO₂ adsorption energy ranging from -2.08 to -2.81 eV, indicating these sites have strong binding with the product molecule and hamper the RWGS reaction, which was also observed in recent study. 48,49 We then introduced defects into the adsorption cluster, namely, one C defect and one Mo defect, respectively, on Mo₂C (Figure 4a), the binding of the CO molecule and the cluster is slightly reduced, with a desorption energy of 2.42 and 2.17 eV, respectively. When two Mo defects were introduced to the cluster (Mo5 and Mo10, Figure 4a), we surprisingly observed a sharp decrease of the desorption energy from 2.57 to 1.76 eV for CO on the identical site (Mo9), and the site becomes the most vulnerable site to the electrophilic attach based on the prediction by Fukui analysis (Figure S6). Similarly, the desorption energy of H₂O on such a site has also been decreased to 0.72 eV. In addition, our DFT results also predicted the CO desorption on an intact metallic Mo@NGn had a similarly small energy of 1.75 eV. These results imply that Mo₂C with dual Mo defects as well as Mo cluster would potentially benefit products escaping during the RWGS reaction.

To reveal the underlying mechanism for the positive effects of the dual Mo defects on CO desorption, the bond strengths between adsorbate and various active sites were first considered, and Mo₂N_vMo@NGn and Mo₂C_vMo@SiO₂ with dual Mo defects were included in the analysis. Surprisingly, the results in Figure S7 reveal that desorption energy has little correlations with the Mo–CO bond strength. Nevertheless, we observed significant changes of the local

electronic spin (magnetization) before and after the CO adsorption onto Mo₂C_vMo@NGn, although the net spin for the whole system is negligible throughout the desorption, and the magnetization for the adsorption site (Mo9) is also nearly zero during the interaction. In a stark contrast, Mo₂C vMo@ SiO₂ was nonmagnetic but the magnetization reached 1.340 μB after the CO adsorption, in which the magnetization for Mo9 saw an obvious rise to 0.123 μ B as shown in Figure S8. Density of states analysis to atom Mo9 in the defected cluster and C in the CO molecule firmly verifies the origin of magnetic characteristic of Mo₂C_vMo supported on NGn and SiO₂, respectively, after CO adsorption (Figure S8). We then performed more magnetic analysis toward other structures, and the results in Figure 4d point out a positive linear correlation between the desorption energy of CO with the total magnetization density of the binding components of Mo9 and CO, where the major spin is indeed contributed by Mo.

Significantly, our findings reveal that the net spin for M9 is virtually negligible in all of the fresh catalysts, as is the case with the CO molecule. However, varying extents of spin polarization are introduced by the adsorption process. We posit that this is related to the charge transfer from Mo to CO, albeit in small quantities, so as suggested by the partial density of states for C and Mo depicted in Figure S8, indicating that the adsorption energy is predominantly contributed by ionic-like binding. We discovered that the magnetization density at the adsorption site effectively characterizes these interactions and aligns well with the CO desorption energy. The dual Mo defects of Mo5 and Mo10 are found to facilitate the release of CO, with a corresponding decrease in net spin.

The effects of Mo defects on the CO_2 adsorption were further investigated. Two different dual Mo defects (v5 and 10, v9 and v10) were compared with the intact Mo_2C cluster, as shown in Figure 4b. It was found that all three clusters have

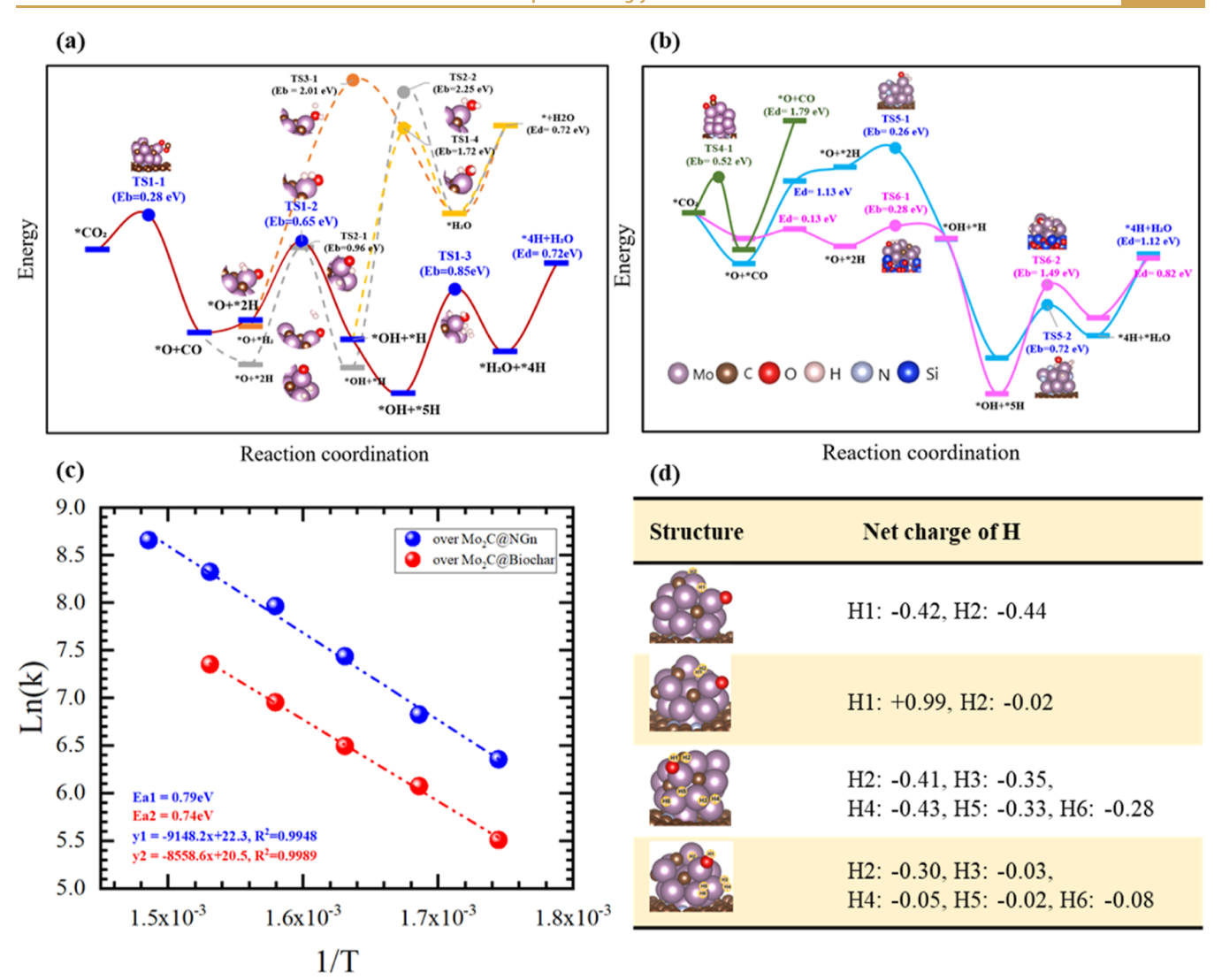


Figure 6. (a,b) Plausible catalytic reaction pathways of CO_2 hydrogenation over $Mo_2C@NGn$, Mo@NGn, $Mo_2N@NGn$, and $Mo_2C@SiO_2$. (c) Apparent activation energy determined by experiments ($mol_{CO_2}/mol_{H_2} = 1:2$, the peak conversion of CO_2 was adjusted under 10%). (d) Atomic charges of the surface H atoms during the hydrogenation reaction.

obvious activation effects on CO₂, wherein the bond angle of CO₂ on the intact Mo₂C sites was 118° and the C=O bond was 1.37 Å. On the cluster with dual-defects of Mo9 and Mo10, the C=O bond was more stretched to 1.40 Å. When it was on the cluster with dual-defects v5 and v10, the molecule was the most polarized with the smallest bond angle of 112°. This indicates the dual-defected Mo₂C@NGn outperforms the intact cluster catalyst for CO₂ activation as well.²² More interestingly, we observed that dissociation of CO₂ on Mo9 v5 and 10 would give rise to the facile desorption of CO, while in other two circumstances, the CO molecule would stay binding with adjacent Mo atoms. The above results have clearly indicated that Mo defects create the original activity for the Mo₂C@NGn cluster in the RWGS reaction. The above conclusion is further evidenced by experimental data. Figure 5 shows the results of X-ray absorption spectroscopy (XAS) for the catalyst samples of Mo₂C@NGn (fresh), Mo₂C@NGn (spent), and Mo₂C@SiO₂, as well as standard samples of Mo foil, MoO₃, and Mo₂C as references. XRD tests were implemented to the sample of Mo₂C@NGn and Mo₂C@ SiO₂ to confirm that the bulk species are entirely Mo₂C, as shown in Figure S9. Figure 5a shows the X-ray absorption

near-edge structure (XANES) spectra of the Mo K-edge for the investigated Mo-based catalysts. Figure 5b shows an average valence estimation for the Mo element in the catalysts and standard samples based on their edge positions. The valence of Mo in $Mo_2C@SiO_2$ was +1.17, close to that of Mo_2C (standard sample), and the valence of Mo was +1.33 in both fresh $Mo_2C@NGn$ and spent $Mo_2C@NGn$. The results imply a lower stoichiometric number of Mo molecules in the NGn-supported Mo_2C catalysts.

We further analyzed the nearest coordination environment for all three samples in comparison with the Mo₂C standard sample, based on the extended X-ray absorption fine structure (EXAFS) data. The detailed fitting paths and results are shown in Figure S10. Figure 5d shows the averaged coordinated number of adjacent elements for the Mo atom. As can be seen, for the Mo₂C standard sample, one central Mo atom had three carbon atoms and 12 Mo in the first nearest neighbor, and when it was loaded on SiO₂, the coordination number of C slightly increased, while the coordination number of Mo saw a slight decrease, implying the existence of Mo defects. When it was over the carbon support of NGn, the increase of C coordination number and the decrease of Mo coordination

number became more obvious, indicating that rich Mo defects have been created on the $Mo_2C@NGn$ during carbonization and that the carbon support is effective to creating more defected sites, which is decisive to the catalytic activity toward the RWGS reaction.

2.3. Reaction Kinetics of Selective Hydrogenation over the Defected Mo-Based Catalysts

Regarding the hydrogenation of CO₂ over Mo₂C vMo@NGn, we considered the Mars-Van Krevelen (MVK) mechanism and the Eley-Rideal (ER) mechanism. Modeling results show that the reaction at the beginning could hardly proceed through the ER mechanism (Figure S11). Figure 6 demonstrates various hydrogenation pathways of CO₂ and the corresponding potential energy barriers based on MVK mechanisms. We observed that CO₂ experienced a small energy barrier of 0.28 eV before the direct dissociative desorption of CO. Three different pathways have been observed for hydrogenation to the surface *O, based on different configurations of adsorbed H2. The most favorable path had an energy barrier of 0.65 eV to produced *OH. The following step of hydrogenation with the only one surface *H needs to overcome energy barriers of at least 1.72 eV for both pathways. However, with additional hydrogen molecules coverage, the energy barrier was decreased by 0.87 eV to generate *H2O, which would further experience an endothermic desorption with the energy of 0.72 eV. In contract, one step hydrogenation of *O to produce *H₂O under the ER mechanism had a much higher energy barrier of 2.01 eV. The hydrogenation pathways of CO2 over other catalysts of Mo₂C_vMo@SiO₂, Mo_vMo@NGn, and Mo₂N_vMo@ NGn were also modeled and are compared in Figure 6b. Over the defected Mo₂C supported on SiO₂, the dissociation of CO₂ and hydrogenation to *O were facile, but hydrogenation to*OH had an energy barrier of 1.49 eV. Over the defected metallic Mo cluster supported on NGn, we found that the dissociation of CO2 was not difficult, while the CO desorption was the potential rate-determining step with an endothermic energy of 1.79 eV. The defected Mo₂N supported on NGn gave rise to smaller energy barriers of 0.28 and 0.72 eV for the two steps hydrogenation, respectively, compared to those over Mo₂C_vMo@NGn; however, the desorption energy of CO was 1.13 eV in the presence of *O.

The DFT modeling results confirm Mo₂C_vMo@NGn to be the best catalyst candidate for the RWGS reaction, with the peak energy barrier of 0.85 eV for the most favorable pathway, and the result has been validated by the apparent activation energy of 0.79 eV determined by the experimental data, as shown in Figure 6c. The results in this study indicate that the peak energy for the RWGS reaction is 0.3 eV lower than that over the single-atom catalyst Mo1@NGn. Besides, we also carried out kinetic analysis for the experiments based on Mo₂C@NBiochar, despite its slightly smaller turn over frequency (TOF) compared to Mo₂C@NGn (Table S12). It demonstrates a lower activation energy in experiments, implying biochar as an alternative carbon support for large-scale applications instead of NGn.

In addition, the above modeling results also reveal that increasing hydrogen coverage would benefit the hydrogenation reaction, and this phenomenon was also observed in other hydrogenation circumstance⁵³ and had been thoroughly investigated in our recent work;²⁹ additional H₂ adsorption is able to adjust the valent electrons of Mo atom and tends to

neutralize the charge of surface *H atoms, promoting the hydrogenation. The conclusion was again verified by the hydrogenation in this study, where we found that only chargeneutral *H atoms were able to launch the hydrogenation, as shown in Figure S13. Interestingly, we noticed that Mo defects also contribute to the selective hydrogenation by neutralizing the *H charge. To clarify this, we carried out further comparative studies regarding the net charge of surface hydrogens over both intact Mo₂C@NGn and Mo₂C_vMo@ NGn. Figure 6 reveals that the defected catalyst always leads to the charge neutrality of the surface *H. In contrast, over the intact cluster, the *H carried obvious negative charges in both circumstances, which would directly hinder the consequent hydrogenation reaction. We therefore conclude that Mo defects in Mo₂C not only contribute to the CO₂ activation and CO liberation but also benefit the following hydrogenations by proper charge adjustment of the surface hydrogen.

3. CONCLUSIONS AND THE PERSPECTIVES

In summary, we have demonstrated the outstanding performance of Mo₂C@NGn in the low-temperature RWGS reaction. The catalyst achieved a CO yield rate of 6.3 g_{CO}/g_{cat}/h and >99% CO selectivity at 400 °C with good stability. Mechanism studies revealed that Mo₂C@NGn outperformed other Mobased catalysts by facilitating the dissociation of CO₂ with nonbarrier liberation of CO, and the peak activation energy for the hydrogenation was around 0.8 eV, superior to the singleatom catalyst of Mo. We conclusively proved that Mo defects in Mo₂C played a key role in driving the catalytic RWGS reaction. We observed that the atomic net spin was a potential descriptor for CO desorption based on a revealed linear correlation. The Mo defects facilitated product desorption by decreasing the magnetization of the adsorption site atom. On the other hand, the defects also neutralized the surface hydrogen charge, which was crucial for selective hydrogenation, in line with the function of increasing H coverage. Moreover, we have demonstrated that a combination of carbon support and carbonization process is an effective strategy for creating rich Mo defects to promote the selective hydrogenation of CO₂ at low temperatures. Biochar, as an alternative support, gains much potential for large-scale applications, given its low cost and wide accessibility.

4. METHODOLOGY

4.1. Materials and Preparation of Catalysts

Materials of ammonium molybdate tetrahydrate $[(NH4)_6Mo_7O_{24}\cdot 4H_2O]$, chromium(III) nitrate nonahydrate $(CrN_3O_9\cdot 9H_2O)$, ammonium tungstate $[(NH_4)-10H_2(W_2O_7)_6]$, nitrogen-doped graphene (NGn), and SiO₂ were supplied by Aladdin Reagents Co., Ltd. The NBiochar was prepared by lignin, urea, and NaHCO₃ with the ratio 1/4/3 of each component; in each batch of preparation, 30 g of mixed feedstock was pyrolyzed in a graphite crucible at 700 °C for 2 h with a ramp of 3 °C/min in N₂. The naturally cooled solid products were then washed by 1 M HNO₃ solution and then with water several times until the pH of the solution was 7. The as-obtained Nbiochar was dried at 60 °C for 24 h before being used as the support in catalyst synthesis. The other batch of Nbiochar was prepared in the same process except the pyrolysis temperature of 800 °C. SiO₂ was milled

and sieved to 0.125-0.250 mm before being used as the support.

50% Mo₂C@NGn catalysts were synthesized by wet impregnation with 50 mg of NGn with aqueous solutions of 92.1 mg of the metal precursor of (NH4)₆Mo₇O₂₄·4H₂O. The impregnation mixtures were stirred within a shaker for 24 h at room temperature (~25 °C). Water was removed by evaporation at 80 °C, and the impregnated support was then dried at 60 °C for 24 h. The sample was then calcined in pure N₂ for 2 h at 500 °C. The metal loading ratio was verified by the inductively coupled plasma (ICP) technique on the Thermo IRIS Intrepid II ICP–OES equipment. Specific surface area and porous information were investigated in the Brunauer–Emmett–Teller test. Relevant physical parameters are summarized in Table S14.

For carbonization before each experiment, the catalysts were pretreated in situ with 20 vol % CH₄/H₂ (total flow rate of 25 mL/min), with a ramp of 10 °C/min to 300 and 2 °C/min to 700 °C, and the temperature was stabilized at 700 °C for an additional 2 h. For reduction, the catalysts were pretreated in situ with 50 vol % H₂/Ar (total flow rate of 20 mL/min) before each experiment, with a ramp of 10 °C/min to 700 °C, and the temperature was held at 700 °C for an additional 2 h. For nitrogenation, the catalysts were pretreated in situ with 50 vol % H₂/N₂ (total flow rate of 20 mL/min) before each experiment, with a ramp of 10 °C/min to 700 °C before the temperature was held at 700 °C for an additional 2 h. Catalysts with various metal loadings and metal species were prepared in an analogous procedure, except that the carbonization temperature for Cr₃C₂ was 850 °C. The as-obtained catalysts are denoted as x% M@NGn, where M is the active species and x is the loading ratio (x = 10, 20, or 50).

4.2. Structural Characterizations

In situ XRD patterns were recorded on a Bruker D8 Advance diffractometer equipped with an Anton Paar XRK-900 furnace operating at 40 kV with Cu K α radiation ($\lambda = 1.5406$ Å) within the range of 20.0-50.0°, using a scanning rate of 0.85°/min. 30 mg of 50% Mo@NGn was exposed to a CH₄/H₂ flow (5 mL/min CH₄ with 20 mL/min H₂) for reduction. After the first XRD collection at room temperature, the temperature was sequentially increased to 300 °C with a ramp of 10 °C/min and then to 700 °C with a ramp of 2 °C/min, during which the XRD measurements were performed every 100 °C before 500 °C and every 20 °C afterward. The temperature was then held at 700 °C for another 6 h, and the XRD measurements were performed every 30 min. When the specimen was cooled to 500 $^{\circ}$ C, the XRD collection was then performed every 30 min in the reaction flow (5 mL/min of CO₂, 10 mL/min of H₂, and 5 mL/min of N₂) for 3 h. The inlet gas was then switched to 10 mL/min H₂ and 10 mL/min Ar for XRD measurements at constant 500 °C at the final 3 h. Ex situ XRD patterns were recorded on a RIGAKU SmartLab X-ray diffractometer with a scanning rate of 2° /min in the range of 20.0° – 80.0° .

High-resolution transmission electron microscopy and EDS element mapping images were obtained with a Talos F200S field-emission high resolution TEM operating at 200 kV, and the information resolution was 0.12 nm. Specimens were prepared by ultrasonic dispersion of catalyst samples in ethanol before the suspension was dropped onto a copper grid. Images of the microstructures of the specimens were acquired. EDS elemental mapping was performed using SUPER-X to determine the existing elements on the sample surface.

XAS was performed at beamline 07 A of the Taiwan photon source (TPS) with the edge energy ranging from 5 to 22 keV. The data of standard samples were provided by TPS. Data processing of XANES and EXAFS was carried out using the Athena software package.

The CO temperature-programmed desorption (CO-TPD) experiments were performed on an Agilent 8860 instrument equipped with a thermal conductivity detector (TCD). Prior to the measurement, 10 mg of the catalyst precursor was loaded in a quartz tube, pretreated at 200 °C under Ar flow (20 mL/ min) for 1 h to remove the adsorbed species on the catalyst surface, and then cooled to 30 °C in pure Ar flow. The catalysts were kept in a CO flow (20 mL/min) for 30 min to ensure saturated adsorption. Afterward, the adsorbed CO on catalysts was removed by pure Ar flow at 30 °C, and then, the CO-TPD process was carried out from 30 to 600 °C at a heating rate of 10 °C/min. The output signal was detected with a TCD. A similar TPD test was carried out from 80 to 600 °C. The difference of the amount for the desorbed CO in above two tests was regarded as weakly adsorbed CO and used for evaluation of the number of active sites on 50% Mo@NGn for the RWGS reaction.

4.3. Catalytic Performance Tests

CO₂ hydrogenation experiments were carried out in a flow reactor under atmospheric pressure, in which the thermocouple was sleeved by a quartz tube to prevent the additional catalytic effects of the thermocouple on the reactions. In a typical batch, 10 mg of the catalyst precursor was loaded into a quartz tube with an inner diameter of 4 mm and held in place by quartz wool. Before each CO2 hydrogenation experiment, the catalyst was pretreated under the aforementioned conditions. The reactor was then cooled to 300 °C in the pretreatment flow, and the inlet flow was switched to the reactants (i.e., 5 mL/min CO₂, 10 mL/min H₂, and 5 mL/min N₂) for CO₂ hydrogenation. The temperature would remain constant at 300, 400, and 500 °C for reaction at each temperature in sequence with a ramp of 10 °C/min. The activation energy (E_a) was determined according to the Arrhenius equation, based on the CO₂ hydrogenation data between 300 and 400 °C with 20 °C intervals, and the GHSV was adjusted to keep a low conversion of no more than 10%. The gas chromatograph (Agilent 7890B) equipped with a flammable ionization detector (FID) and a TCD were used to analyze the concentration of gas products. The response factor of each reactant and product was calibrated using standard curve methods. The conversion of $CO_2(X_{CO_2})$ is defined as

$$X_{\text{CO}_2} = \frac{F_{\text{CO}_2(\text{inlet})} - F_{\text{CO}_2(\text{outlet})}}{F_{\text{CO}_2(\text{inlet})}} = \frac{\frac{C_{\text{CO}_2(\text{inlet})}}{C_{\text{N}_2(\text{inlet})}} - \frac{C_{\text{CO}_2(\text{outlet})}}{C_{\text{N}_2(\text{outlet})}}}{\frac{C_{\text{CO}_2(\text{inlet})}}{C_{\text{N}_2(\text{inlet})}}}$$
(1)

The selectivity of CO (S_{CO}) is defined as

$$S_{\text{CO}} = \frac{F_{\text{CO(outlet)}}}{F_{\text{CO(outlet)}} + F_{\text{CH}_{4}(\text{outlet)}}} = \frac{\frac{\frac{C_{\text{CO(outlet)}}}{C_{\text{N}_{2}(\text{outlet)}}}}{\frac{C_{\text{CO(outlet)}}}{C_{\text{N}_{2}(\text{outlet)}}} + \frac{C_{\text{CH}_{4}(\text{outlet)}}}{C_{\text{N}_{2}(\text{outlet)}}}}$$
(2)

where *F* is the flow rate of reactants or products (mol/min) and *C* is the concentration of reactants or products (%).

For each temperature test, an averaged value of 5 GC-FID/TCD data was used in this study. Exclusion of the reverse

Boulouard reaction was confirmed by detection of the CO yield with an inactive catalyst, as shown in Table S16.

4.4. DFT Calculations

The first-principles density functional theory plus dispersion calculations were implemented in the Vienna Ab initio Simulation Package (VASP) with dispersion corrections by the D3 method of Grimme. The generalized gradient corrected approximation⁵⁴ treated by the Perdew-Burke-Ernzerhof exchange-correlation potential was used to calculate the exchange-correlation energy. 55-57 The Projector-Augmented-Wave (PAW) pseudopotential was employed as the scheme in the representation of reciprocal space for all the elements.^{58,59} The plane-wave cutoff energy was set to 450 eV for all the calculations. The Brillouin zone was sampled using a $2 \times 2 \times 1$ and $4 \times 4 \times 1$ Monkhorst–Pack k-point with a smearing of 0.1 eV for respective geometry optimization and static electron structures calculation. Independence tests of both cutoff energy and k-points were carried out, as shown in Figure S17. Spin polarization has been considered, and the self-consistent field tolerance was set to 10⁻⁴ eV/atom. All the modeling was performed with a convergence threshold of 0.03 eV/Å on maximum force. No symmetry constraint was used for any modeling. The computational method is believed to give high precision results and has been validated by experimental data in describing graphene-based materials in our recent work and Mo lattice.²⁹ In this work, the model predicted the lattice constant of the Mo₂C lattice to be a = 4.72 Å, b = 5.20 Å, and c= 6.02 Å, in agreement with the experimental data of a = 4.74Å, b = 5.21 Å, and c = 6.03 Å, ⁶⁰ as shown in Table S18.

All the models were based on a three-layer $p(4 \times 4)$ supercell of four nitrogen-doped graphene (100) facet. A 15 Å vacuum region was created above the top layer of the graphite facet. MedeA 3.1.0 was used for model establishment and pseudopotential assembly for the calculation. Geometry optimization was implemented to each model before the energy was calculated. Energy of all of the geometries was calculated at 0 K in the DFT investigation with corrections of zero point energy based on frequency analysis. Bader charge was calculated for atomic electron analysis. 61,62 The adsorption energy (E_{ad}) and desorption energy (E_{des}) are determined by eqs 3 and 4, where E_{catalyst} , $E_{\text{adsorbate}}$, and $E_{\text{adsorbate/catalyst}}$ are the total energies of clean catalyst, free adsorbate molecule, and catalyst with adsorbed molecule, respectively. The transition state (TS) was completely determined by the algorithm of climbing image nudged elastic band combining with the dimer method and confirmed by sole imaginary frequencies (Figure S15). The energy barrier of a reaction (E_{barrier}) was determined by the difference between the energies of the TS and reactant, as shown in eq 5, where the $E_{\text{transition}}$ state and reactant are the total energies of the TS and reactant of a reaction, respectively.

$$E_{\rm ad} = E_{\rm adsorbate/catalyst} - (E_{\rm catalyst} + E_{\rm adsorbate})$$
 (3)

$$E_{\rm des} = (E_{\rm catalyst} + E_{\rm adsorbate}) - E_{\rm adsorbate/catalyst}$$
 (4)

$$E_{\text{barrier}} = E_{\text{transitionstate}} - E_{\text{reactant}} \tag{5}$$

The electron density difference was determined by eq 6.

$$\Delta \rho = \rho_{\text{adsorbate@NGn}} - (\rho_{\text{adsorbate}} + \rho_{\text{NGn}})$$
 (6

where $\rho_{adsorbate@NGn}$ is the electron density of the whole adsorbate + adsorbent system, and $\rho_{adsorbate}$ and ρ_{NGn} are the

unperturbed electron densities of the adsorbate and the adsorbent structure, respectively.

4.5. AIMD Modeling

The AIMD modeling was implemented to confirm the stability of the catalyst unit, within the canonical (NVT) ensemble in VASP 5.4.4, using the model established in this work. The time step was 0.5 fs, and the testing temperature was 1000 K.

ASSOCIATED CONTENT

supporting Information

The Supporting Information is available free of charge at https://pubs.acs.org/doi/10.1021/jacsau.3c00206.

Details of the catalytic behavior of reported catalysts in the literature and other mentioned catalysts in the article, cluster, and support interactions; Fukui analysis; bond strength analysis and electronic spin analysis; electronic spin of the clusters; EXAFS fittings; TOF of reaction; charge analysis of surface *H atoms; physical properties of the catalysts; TS frequencies; reaction test with inert catalyst; independence test of cutoff energy and *k*-points; and the validation of the computational method (PDF)

AUTHOR INFORMATION

Corresponding Authors

Bin Yang — Center for Combustion Energy, Key Laboratory for Thermal Science and Power Engineering of Ministry of Education, International Joint Laboratory on Low Carbon Clean Energy Innovation, Tsinghua University, Beijing 100084, China; orcid.org/0000-0001-7333-0017; Email: byang@tsinghua.edu.cn

Binhang Yan — Department of Chemical Engineering, Tsinghua University, Beijing 100084, China; ⊚ orcid.org/ 0000-0003-2833-8022; Email: binhangyan@ tsinghua.edu.cn

Kai Hong Luo — Center for Combustion Energy, Key
Laboratory for Thermal Science and Power Engineering of
Ministry of Education, International Joint Laboratory on Low
Carbon Clean Energy Innovation, Tsinghua University,
Beijing 100084, China; Department of Mechanical
Engineering, University College London, London WC1E 7JE,
U.K.; orcid.org/0000-0003-4023-7259; Email: k.luo@
ucl.ac.uk

Authors

Jiajun Zhang — National Engineering Research Center of Green Recycling for Strategic Metal Resources, Institute of Process Engineering, Chinese Academy of Sciences, Beijing 100190, China; Center for Combustion Energy, Key Laboratory for Thermal Science and Power Engineering of Ministry of Education, International Joint Laboratory on Low Carbon Clean Energy Innovation, Tsinghua University, Beijing 100084, China

Kai Feng – Department of Chemical Engineering, Tsinghua University, Beijing 100084, China

Zhengwen Li – Department of Chemical Engineering, Tsinghua University, Beijing 100084, China

Complete contact information is available at: https://pubs.acs.org/10.1021/jacsau.3c00206

Author Contributions

J. Zhang: conceptualization, methodology, investigations—experiments, DFT modeling, AIMD modeling, writing—original draft and editing, funding acquisition, and project management. K. Feng and Z. Li: investigation—experiments. B. Yan: supervision and writing—review and editing. B. Yang: supervision, funding acquisition, and writing—review and editing. K. H. Luo.: research supervision, writing—review and editing, and provision of supercomputing resources. CRediT: Jiajun Zhang conceptualization, data curation, formal analysis, funding acquisition, investigation, methodology, project administration.

Notes

The authors declare no competing financial interest.

ACKNOWLEDGMENTS

The authors acknowledge the financial support from the National Natural Science Foundation of China (NSFC, grant no. 52206156 and 52076116), the Fellowship of China Postdoctoral Science Foundation (2021M701851), and "Shuimu Scholar" scheme at Tsinghua University (2019SM127). The work is also supported by the Tsinghua-Toyota Joint Research Fund. Support from the UK Engineering and Physical Sciences Research Council under the project "UK Consortium on Mesoscale Engineering Sciences (UK-COMES)" (grant nos. EP/R029598/1 and EP/X035875/1) is gratefully acknowledged. This work made use of computational support by CoSeC, the Computational Science Centre for Research Communities, through UKCOMES.

REFERENCES

- (1) Dokania, A.; Ould-Chikh, S.; Ramirez, A.; Cerrillo, J. L.; Aguilar, A.; Russkikh, A.; Alkhalaf, A.; Hita, I.; Bavykina, A.; Shterk, G.; Wehbe, N.; Prat, A.; Lahera, E.; Castaño, P.; Fonda, E.; Hazemann, J. L.; Gascon, J. Designing a Multifunctional Catalyst for the Direct Production of Gasoline-Range Isoparaffins from CO2. *JACS Au* 2021, 1 (11), 1961–1974.
- (2) Paykani, A.; Chehrmonavari, H.; Tsolakis, A.; Alger, T.; Northrop, W. F.; Reitz, R. D. Synthesis Gas as a Fuel for Internal Combustion Engines in Transportation. *Prog. Energy Combust. Sci.* **2022**, *90* (February), 100995.
- (3) Du, P.; Qi, R.; Zhang, Y.; Gu, Q.; Xu, X.; Tan, Y.; Liu, X.; Wang, A.; Zhu, B.; Yang, B.; Zhang, T. Single-Atom-Driven Dynamic Carburization over Pd1–FeOx Catalyst Boosting CO2 Conversion. *Chem* **2022**, 8 (12), 3252–3262.
- (4) Zhang, R.; Wang, X.; Wang, K.; Wang, H.; Liu, L.; Wu, X.; Geng, B.; Chu, X.; Song, S.; Zhang, H. Synergism of Ultrasmall Pt Clusters and Basic La 2 O 2 CO 3 Supports Boosts the Reverse Water Gas Reaction Efficiency. *Adv. Energy Mater.* **2023**, *13*, 2203806.
- (5) Wang, L.; Zhang, L.; Zhang, L.; Yun, Y.; Wang, K.; Yu, B.; Zhao, X.; Yang, F. Direct Environmental TEM Observation of Silicon Diffusion-Induced Strong Metal-Silica Interaction for Boosting CO2 Hydrogenation. *Nano Res.* **2022**, *16*, 2209–2217.
- (6) Ziemba, M.; Weyel, J.; Hess, C. Elucidating the Mechanism of the Reverse Water—Gas Shift Reaction over Au/CeO2 Catalysts Using Operando and Transient Spectroscopies. *Appl. Catal., B* **2022**, 301 (October2021), 120825.
- (7) Chen, L.; Unocic, R. R.; Hoffman, A. S.; Hong, J.; Braga, A. H.; Bao, Z.; Bare, S. R.; Szanyi, J. Unlocking the Catalytic Potential of TiO2-Supported Pt Single Atoms for the Reverse Water-Gas Shift Reaction by Altering Their Chemical Environment. *JACS Au* **2021**, *1* (7), 977–986.
- (8) Kim, G.; Shin, S.; Choi, Y.; Kim, J.; Kim, G.; Kim, K.-J.; Lee, H. Gas-Permeable Iron-Doped Ceria Shell on Rh Nanoparticles with High Activity and Durability. *JACS Au* 2022, 2 (5), 1115–1122.

- (9) Lin, S.; Wang, Q.; Li, M.; Hao, Z.; Pan, Y.; Han, X.; Chang, X.; Huang, S.; Li, Z.; Ma, X. Ni–Zn Dual Sites Switch the CO 2 Hydrogenation Selectivity via Tuning of the d-Band Center. *ACS Catal.* **2022**, *12* (6), 3346–3356.
- (10) Sinehbaghizadeh, S.; Saptoro, A.; Mohammadi, A. H. CO2 hydrate properties and applications: A state of the art. *Nat. Commun.* **2022**, 93 (1), 101026.
- (11) Wei, A.; Zhang, R.; Qin, Y.; Wang, H.; Zhu, X.; Ge, Q. Theoretical Insight into Tuning CO₂ Methanation and Reverse Water Gas Shift Reactions on MoO_x-Modified Ni Catalysts. *J. Phys. Chem. C* **2022**, *126* (42), *18078*–*18089*.
- (12) Li, W.; Nie, X.; Yang, H.; Wang, X.; Polo-Garzon, F.; Wu, Z.; Zhu, J.; Wang, J.; Liu, Y.; Shi, C.; Song, C.; Guo, X. Crystallographic Dependence of CO2 Hydrogenation Pathways over HCP-Co and FCC-Co Catalysts. *Appl. Catal., B* **2022**, *315* (May), 121529.
- (13) Xing, S.; Turner, S.; Fu, D.; van Vreeswijk, S.; Liu, Y.; Xiao, J.; Oord, R.; Sann, J.; Weckhuysen, B. M. Silicalite-1 Layer Secures the Bifunctional Nature of a CO 2 Hydrogenation Catalyst. *JACS Au* **2023**, 3 (4), 1029–1038.
- (14) Li, K.; Li, X.; Li, L.; Chang, X.; Wu, S.; Yang, C.; Song, X.; Zhao, Z. J.; Gong, J. Nature of Catalytic Behavior of Cobalt Oxides for CO2 Hydrogenation. *JACS Au* **2023**, 3 (2), 508–515.
- (15) Li, Y.; Zhao, Z.; Lu, W.; Zhu, H.; Sun, F.; Mei, B.; Jiang, Z.; Lyu, Y.; Chen, X.; Guo, L.; Wu, T.; Ma, X.; Meng, Y.; Ding, Y. Single-Atom Co-N-C Catalysts for High-Efficiency Reverse Water-Gas Shift Reaction. *Appl. Catal., B* **2023**, 324 (November 2022), 122298.
- (16) Cao, F.; Xiao, Y.; Zhang, Z.; Li, J.; Xia, Z.; Hu, X.; Ma, Y.; Qu, Y. Influence of Oxygen Vacancies of CeO2 on Reverse Water Gas Shift Reaction. *J. Catal.* **2022**, 414, 25–32.
- (17) Pajares, A.; Prats, H.; Romero, A.; Viñes, F.; de la Piscina, P. R.; Sayós, R.; Homs, N.; Illas, F. Critical Effect of Carbon Vacancies on the Reverse Water Gas Shift Reaction over Vanadium Carbide Catalysts. *Appl. Catal., B* **2020**, *267* (February), 118719.
- (18) Zhang, Q.; Pastor-Pérez, L.; Wang, Q.; Ramirez Reina, T. Conversion of CO2 to Added Value Products via RWGS Using Fe-Promoted Catalysts: Carbide, Metallic Fe or a Mixture? *J. Energy Chem.* **2022**, *66*, *635–646*.
- (19) Pahija, E.; Panaritis, C.; Gusarov, S.; Shadbahr, J.; Bensebaa, F.; Patience, G.; Boffito, D. C. Experimental and Computational Synergistic Design of Cu and Fe Catalysts for the Reverse Water–Gas Shift: A Review. ACS Catal. 2022, 12 (12), 6887–6905.
- (20) Li, Y.; Fang, Z.; Zhou, H.; Li, Y.; Wang, B.; Huang, S.; Lin, W.; Chen, W. K.; Zhang, Y. Theoretical Insights into Synergistic Effects at Cu/TiC Interfaces for Promoting CO2Activation. ACS Omega 2021, 6 (41), 27259–27270.
- (21) Morales-Salvador, R.; Gouveia, J. D.; Morales-García, Á.; Viñes, F.; Gomes, J. R. B.; Illas, F. Carbon Capture and Usage by MXenes. ACS Catal. 2021, 11 (17), 11248–11255.
- (22) Jimenez-Orozco, C.; Figueras, M.; Flórez, E.; Viñes, F.; Rodriguez, J. A.; Illas, F. Effect of Nanostructuring on the Interaction of CO 2 with Molybdenum Carbide Nanoparticles. *Phys. Chem. Chem. Phys.* **2022**, 24 (27), 16556–16565.
- (23) Figueras, M.; Gutiérrez, R. A.; Viñes, F.; Ramírez, P. J.; Rodriguez, J. A.; Illas, F. Supported Molybdenum Carbide Nanoparticles as Hot Hydrogen Reservoirs for Catalytic Applications. *J. Phys. Chem. Lett.* **2020**, *11* (19), 8437–8441.
- (24) Zhang, Q.; Bown, M.; Pastor-Pérez, L.; Duyar, M. S.; Reina, T. R. CO 2 Conversion via Reverse Water Gas Shift Reaction Using Fully Selective Mo—P Multicomponent Catalysts. *Ind. Eng. Chem. Res.* **2022**, *61* (34), 12857—12865.
- (25) Zhou, H.; Chen, Z.; Kountoupi, E.; Tsoukalou, A.; Abdala, P. M.; Florian, P.; Fedorov, A.; Müller, C. R. Two-Dimensional Molybdenum Carbide 2D-Mo2C as a Superior Catalyst for CO2 Hydrogenation. *Nat. Commun.* **2021**, *12* (1), 5510.
- (26) Wu, Y.; Xie, Z.; Gao, X.; Zhou, X.; Xu, Y.; Fan, S.; Yao, S.; Li, X.; Lin, L. The Highly Selective Catalytic Hydrogenation of CO2 to CO over Transition Metal Nitrides. *Chin. J. Chem. Eng.* **2022**, *43*, 248–254.

- (27) Liu, H.-X.; Li, J.-Y.; Qin, X.; Ma, C.; Wang, W.-W.; Xu, K.; Yan, H.; Xiao, D.; Jia, C.-J.; Fu, Q.; Ma, D. Ptn–Ov Synergistic Sites on MoOx/γ-Mo2N Heterostructure for Low-Temperature Reverse Water–Gas Shift Reaction. *Nat. Commun.* **2022**, *13* (1), 5800.
- (28) Feng, K.; Tian, J.; Zhang, J.; Li, Z.; Chen, Y.; Luo, K. H.; Yang, B.; Yan, B. Dual Functionalized Interstitial N Atoms in Co 3 Mo 3 N Enabling CO 2 Activation. ACS Catal. 2022, 12 (8), 4696–4706.
- (29) Zhang, J.; Yang, B.; Luo, K. H. Unveiling the Mechanism of Controllable CO2 Hydrogenation by Group VIB Metal Single Atom Anchored on N-Doped Graphite: A Density Functional Theory Study. *Int. J. Hydrogen Energy* **2022**, *47* (97), 40972–40985.
- (30) Jiang, Y.; Sung, Y.; Choi, C.; Joo Bang, G.; Hong, S.; Tan, X.; Wu, T. S.; Soo, Y. L.; Xiong, P.; Meng-Jung Li, M.; Hao, L.; Jung, Y.; Sun, Z. Single-Atom Molybdenum-N3 Sites for Selective Hydrogenation of CO2 to CO. *Angew. Chem., Int. Ed.* **2022**, *61* (37), No. e202203836, DOI: 10.1002/anie.202203836.
- (31) Kunisada, Y.; Sakaguchi, N. Chemical Modification of Graphene for Atomic-Scale Catalyst Supports. *Nano Express* **2022**, 3. 042001.
- (32) Nie, Y.; Deng, J.; Chen, S.; Wei, Z. Promoting Stability and Activity of PtNi/C for Oxygen Reduction Reaction via Polyaniline-Confined Space Annealing Strategy. *Int. J. Hydrogen Energy* **2019**, 44 (12), 5921–5928.
- (33) Mao, S.; Wang, C.; Wang, Y. The Chemical Nature of N Doping on N Doped Carbon Supported Noble Metal Catalysts. *J. Catal.* **2019**, 375, 456–465.
- (34) Nityashree, N.; Price, C. A. H.; Pastor-Perez, L.; Manohara, G. V.; Garcia, S.; Maroto-Valer, M. M.; Reina, T. R. Carbon Stabilised Saponite Supported Transition Metal-Alloy Catalysts for Chemical CO2 Utilisation via Reverse Water-Gas Shift Reaction. *Appl. Catal., B* **2020**, *261*, 118241.
- (35) Rudy, E.; Windisch, S.; Stosick, A. J.; Hoffman, J. R. The Constitution of Binary Molybdenum-Carbon Alloys. *Trans. Metall. Soc. AIME* **1967**, 239, 1247–1267.
- (36) Lv, C.; Yang, Q.; Xu, S.; Yuan, L.; Huang, Z.; Ren, Z.; Luo, J.; Wang, S.; Zhang, C. The in Situ Removal of Surface Molybdenum Oxide for Making Binder-Free Porous Mo 1.98 C 1.02 Film a More Efficient Electrocatalyst for Alkaline Rather than Acidic Hydrogen Production. Sustainable Energy Fuels 2021, 5 (13), 3373–3381.
- (37) Lv, C.; Lou, P.; Shi, C.; Wang, R.; Fu, Y.; Gao, L.; Wang, S.; Li, Y.; Zhang, C. Efficient Hydrogen Production via Sunlight-Driven Thermal Formic Acid Decomposition over a Porous Film of Molybdenum Carbide. *J. Mater. Chem. A* **2021**, *9* (39), 22481–22488.
- (38) Ettmayer, P. The System Molybdenum-Nitrogen. *Monatsh. Chem.* **1970**, *101* (1), 127–140.
- (39) Naghdi, S.; Rhee, K. Y.; Kim, M. T.; Jaleh, B.; Park, S. J. Atmospheric Chemical Vapor Deposition of Graphene on Molybdenum Foil at Different Growth Temperatures. *Carbon Lett.* **2016**, *18*, 37–42.
- (40) Ji, J.; Aleisa, R. M.; Duan, H.; Zhang, J.; Yin, Y.; Xing, M. Metallic Active Sites on MoO2(110) Surface to Catalyze Advanced Oxidation Processes for Efficient Pollutant Removal. *iScience* **2020**, 23 (2), 100861.
- (41) Pan, W.; Tian, R.; Jin, H.; Guo, Y.; Zhang, L.; Wu, X.; Zhang, L.; Han, Z.; Liu, G.; Li, J.; Rao, G.; Wang, H.; Chu, W. Structure, Optical, and Catalytic Properties of Novel Hexagonal Metastable h-MoO 3 Nano- and Microrods Synthesized with Modified Liquid-Phase Processes. *Chem. Mater.* **2010**, 22 (22), 6202–6208.
- (42) Liu, X.; Xing, C.; Yang, F.; Liu, Z.; Wang, Y.; Dong, T.; Zhao, L.; Liu, H.; Zhou, W. Strong Interaction over Ru/Defects-Rich Aluminium Oxide Boosts Photothermal CO 2 Methanation via Microchannel Flow-Type System. *Adv. Energy Mater.* **2022**, *12* (31), 2201009.
- (43) Dewangan, N.; Ashok, J.; Sethia, M.; Das, S.; Pati, S.; Kus, H.; Kawi, S. Cobalt-Based Catalyst Supported on Different Morphologies of Alumina for Non-oxidative Propane Dehydrogenation: Effect of Metal Support Interaction and Lewis Acidic Sites. *ChemCatChem* **2019**, *11* (19), 4923–4934.

- (44) Chen, J.; Wang, H.; Wang, Z.; Mao, S.; Yu, J.; Wang, Y.; Wang, Y. Redispersion of Mo-Based Catalysts and the Rational Design of Super Small-Sized Metallic Mo Species. *ACS Catal.* **2019**, *9* (6), 5302–5307.
- (45) Marquart, W.; Raseale, S.; Prieto, G.; Zimina, A.; Sarma, B. B.; Grunwaldt, J.-D.; Claeys, M.; Fischer, N. CO 2 Reduction over Mo 2 C-Based Catalysts. *ACS Catal.* **2021**, *11* (3), 1624–1639.
- (46) Nan, B.; Fu, Q.; Yu, J.; Shu, M.; Zhou, L.-L.; Li, J.; Wang, W.-W.; Jia, C.-J.; Ma, C.; Chen, J.-X.; Li, L.; Si, R. Unique Structure of Active Platinum-Bismuth Site for Oxidation of Carbon Monoxide. *Nat. Commun.* **2021**, *12* (1), 3342.
- (47) Yang, Y.; Tan, M.; Garcia, A.; Zhang, Z.; Lin, J.; Wan, S.; McEwen, J.-S.; Wang, S.; Wang, Y. Controlling the Oxidation State of Fe-Based Catalysts through Nitrogen Doping toward the Hydrodeoxygenation of m -Cresol. ACS Catal. 2020, 10 (14), 7884–7893.
- (48) Liu, X.; Kunkel, C.; Ramírez de la Piscina, P.; Homs, N.; Viñes, F.; Illas, F. Effective and Highly Selective CO Generation from CO_2 Using a Polycrystalline α -Mo₂C Catalyst. ACS Catal. **2017**, 7 (7), 4323–4335.
- (49) Li, J.; Liu, J.; Yang, B. Insights into the Adsorption/Desorption of CO2 and CO on Single-Atom Fe-Nitrogen-Graphene Catalyst under Electrochemical Environment. *J. Energy Chem.* **2021**, *53*, 20–25
- (50) Ram, S.; Lee, S. C.; Bhattacharjee, S. Adsorption Energy Scaling Relation on Bimetallic Magnetic Surfaces: Role of Surface Magnetic Moments. *Phys. Chem. Chem. Phys.* **2020**, 22 (32), 17960–17968.
- (51) Wu, P.; Huang, M. Investigation of Adsorption Behaviors, and Electronic and Magnetic Properties for Small Gas Molecules Adsorbed on Pt-Doped Arsenene by Density Functional Calculations. *RSC Adv.* **2023**, *13* (6), 3807–3817.
- (52) Dang, Q.; Tang, S.; Liu, T.; Li, X.; Wang, X.; Zhong, W.; Luo, Y.; Jiang, J. Regulating Electronic Spin Moments of Single-Atom Catalyst Sites via Single-Atom Promoter Tuning on S-Vacancy MoS2for Efficient Nitrogen Fixation. *J. Phys. Chem. Lett.* **2021**, *12* (34), 8355–8362.
- (53) Figueras, M.; Gutiérrez, R. A.; Viñes, F.; Ramírez, P. J.; Rodriguez, J. A.; Illas, F. Supported Molybdenum Carbide Nanoparticles as an Excellent Catalyst for CO 2 Hydrogenation. *ACS Catal.* **2021**, *11* (15), 9679–9687.
- (54) Perdew, J. P.; Burke, K.; Ernzerhof, M. Generalized Gradient Approximation Made Simple. *Phys. Rev. Lett.* **1996**, 77 (18), 3865–3868.
- (55) Grimme, S. Semiempirical GGA-Type Density Functional Constructed with a Long-Range Dispersion Correction. *J. Comput. Chem.* **2006**, 27 (15), 1787–1799.
- (56) Lebedeva, İ. V.; Lebedev, A. V.; Popov, A. M.; Knizhnik, A. A. Comparison of Performance of van Der Waals-Corrected Exchange-Correlation Functionals for Interlayer Interaction in Graphene and Hexagonal Boron Nitride. *Comput. Mater. Sci.* **2017**, *128*, 45–58.
- (57) Politi, J. R. D. S.; Viñes, F.; Rodriguez, J. A.; Illas, F. Atomic and Electronic Structure of Molybdenum Carbide Phases: Bulk and Low Miller-Index Surfaces. *Phys. Chem. Chem. Phys.* **2013**, *15* (30), 12617.
- (58) Lejaeghere, K.; Van Speybroeck, V.; Van Oost, G.; Cottenier, S. Error Estimates for Solid-State Density-Functional Theory Predictions: An Overview by Means of the Ground-State Elemental Crystals. *Crit. Rev. Solid State Mater. Sci.* **2014**, *39* (1), 1–24.
- (59) Pickard, C. J.; Winkler, B.; Chen, R. K.; Payne, M. C.; Lee, M. H.; Lin, J. S.; White, J. A.; Milman, V.; Vanderbilt, D. Structural Properties of Lanthanide and Actinide Compounds within the Plane Wave Pseudopotential Approach. *Phys. Rev. Lett.* **2000**, *85* (24), 5122–5125.
- (60) Epicier, T.; Dubois, J.; Esnouf, C.; Fantozzi, G.; Convert, P. Neutron Powder Diffraction Studies of Transition Metal Hemicarbides M2C1—II. In Situ High Temperature Study on W2C1—and Mo2C1. *Acta Metall.* **1988**, *36* (8), 1903—1921.
- (61) Tang, W.; Sanville, E.; Henkelman, G. A Grid-Based Bader Analysis Algorithm without Lattice Bias. *J. Phys.: Condens. Matter* **2009**, *21* (8), 084204.

(62) Henkelman, G.; Arnaldsson, A.; Jónsson, H. A Fast and Robust Algorithm for Bader Decomposition of Charge Density. *Comput. Mater. Sci.* **2006**, *36* (3), 354–360.

